Prompt gamma-ray burst emission from internal shocks – new insights

S. k. Minhajur Rahaman [1]★ Jonathan Granot [1,2,3] and Paz Beniamini [1,2,3]

[1]*Astrophysics Research Center of the Open University (ARCO), The Open University of Israel, P.O. Box 808, Raánana 4353701, Israel*
[2]*Department of Natural Sciences, The Open University of Israel, P.O. Box 808, Ra'anana 4353701, Israel*
[3]*Department of Physics, The George Washington University, 725 21st Street NW, Washington, DC 20052, USA*

ABSTRACT

Internal shocks are a leading candidate for the dissipation mechanism that powers the prompt γ-ray emission in gamma-ray bursts (GRBs). In this scenario a compact central source produces an ultra-relativistic outflow with varying speeds, causing faster parts or shells to collide with slower ones. Each collision produces a pair of shocks – a forward shock (FS) propagating into the slower leading shell and a reverse shock (RS) propagating into the faster trailing shell. The RS's lab-frame speed is always smaller, while the RS is typically stronger than the FS, leading to different conditions in the two shocked regions that both contribute to the observed emission. We show that optically thin synchrotron emission from both (weaker FS + stronger RS) can naturally explain key features of prompt GRB emission such as the pulse shapes, time evolution of the νF_ν peak flux and photon energy, and the spectrum. Particularly, it can account for two features commonly observed in GRB spectra: (i) a sub-dominant low-energy spectral component (often interpreted as 'photospheric'-like), or (ii) a doubly broken power-law spectrum with the low-energy spectral slope approaching the slow-cooling limit. Both features can be obtained while maintaining high-overall radiative efficiency without any fine tuning of the physical conditions.

Key words: hydrodynamics – relativistic processes – shock waves – (transients:) gamma-ray bursts.

1 INTRODUCTION

Internal shocks are invoked in a variety of astrophysical transients. They are a leading model for internal energy dissipation in the prompt-emission phase of gamma-ray bursts (GRBs; Rees & Meszaros 1994; Kobayashi, Piran & Sari 1997; Sari & Piran 1997; Daigne & Mochkovitch 1998). In the prompt GRB internal shocks model, a compact central source launches an ultra-relativistic outflow of plasma with a varying velocity. At some distance from the source the faster parts of the outflow overtake and collide with the slower parts of the outflow.

Few studies (e.g. Daigne & Mochkovitch 1998; Spada, Panaitescu & Mészáros 2000; Guetta, Spada & Waxman 2001; Bošnjak, Daigne & Dubus 2009; Bustamante et al. 2017; Rudolph et al. 2022, 2023) have constructed prompt GRB light curves adopting a 'ballistic approach' rather than solving for the hydrodynamic equations of shock propagation. In this approach colliding shells are divided into discrete infinitely thin elements, a plastic collision of pairs of these discrete elements gives rise to a merged shell which again collides with another element and the process repeats. The internal energy dissipated in each collision of discrete elements is assigned to a forward shock (FS) if the Lorentz factor (hereafter LF, Γ) of the merged shell is closer to the slowly moving shell and vice versa. While this provides useful approximation for the LF of the shocked material and internal energy dissipation, this approach only provides a crude estimate for the location of the shock fronts. As

we will show it is the relative location of the shock fronts and the different shock strengths that dictate the diversity of the light curves and the shape of the spectra. The ballistic approach washes away these features [see Appendix B (available as online supplementary material) for comparison of the light curves for the ballistic and our hydrodynamic approach].

Genet & Granot (2009) parametrized the propagation of a single shock front assuming the same LF as the shocked matter, and emission between radii R_o and R_f (building upon Granot 2005; Granot, Cohen-Tanugi & Silva 2008). They found an analytic solution for the observed emission (light curves and spectra), using integration over the equal arrival time surface (EATS) for a Band function emission spectrum. That work forms the foundation of this Letter. We make the following refinements: (i) we consider both shock fronts and estimate their LFs, R_o, and R_f using the central source parameters, (ii) we account for the different LFs of each shock front and its shocked emitting matter.

To achieve efficient energy dissipation in internal shocks, the magnetization of the colliding shells cannot be too high. Moreover, the magnetization of the two colliding shells is typically expected to be comparable, as they are part of the same outflow [unlike the external forward and reverse shocks (RS) that form as the ejecta is decelerated by the external medium]. A useful approach is to consider a single collision where the faster (trailing) and slower (leading) parts of the outflow are approximated as two discrete uniform cold shells. Post collision, a contact discontinuity (CD) forms between the shells and a pair of shocks is launched. The slower (leading) shell is shocked by a FS while the faster (trailing) shell is shocked by the RS. The

★ E-mail: rahaman.minhajur93@gmail.com

shocks dissipate part of the outflow's kinetic energy into internal energy. The RS front's lab-frame speed is always smaller than that of the FS front. Moreover, the RS is typically stronger than the FS, which leads to different conditions in the two shocked regions, both of which contribute to the observed emission.

The present study is the first prompt GRB internal shocks modelling to self-consistently account for both shock fronts. In our treatment, we solve the hydrodynamics for shock propagation of both shocks and supplant it by calculating the observed optically thin synchrotron emission through integration over the EATS for each shock, and adding these two contributions.

This letter is structured as follows. Section 2 describes the hydrodynamical setup for shock propagation, the particulars of the synchrotron emission process and the calculation of the observed radiation. Section 3 describes the light curves (pulse morphology), the temporal evolution of the instantaneous spectra and properties of the time-integrated spectrum. Section 4 summarizes our key findings.

2 THE BASIC SETUP OF OUR MODEL

Here, we describe the basic setup of (i) the shock hydrodynamics in the lab frame (Section 2.1), (ii) the prescription for the underlying emission mechanism in the comoving frame of the shocked fluid (Section 2.2), and (iii) details of the EATS in the observer frame, used for calculating the observed radiation (Section 2.3).

Our analysis employs the following three reference frames: (i) the lab frame associated with the central source, (ii) the local comoving frame of the shocked fluid, and (iii) the observer frame of an observer receiving the photons. Frames (i) and (iii) are essentially the same (up to cosmological corrections), but refer to the photon emission (or lab-frame) time t and arrival time T at the observer, respectively. Quantities in the comoving frame are denoted with primes.

2.1 Hydrodynamics of shock propagation

Rahaman, Granot & Beniamini (2023; hereafter Paper I) provide an in-depth analysis of the 1D shock hydrodynamics post-collision. Here, we summarize some key results for a collision of ultra-relativistic shells, relevant to our case. Observations suggest that the peak flux of the prompt GRB pulses from a given burst do not vary considerably. This provides a particularly good motivation for assuming a constant source power. Further, it is found that the duration of the prompt pulses are similar to the separation of the pulses (Nakar & Piran 2002). This gives good motivation for similar shell ejection and source inactivity time-scales.

A central source of constant (isotropic equivalent) power L ejects two discrete cold and unmagnetized shells (S1, S4) over activity time-scales (t_{on1}, t_{on4}) separated by an inactivity time t_{off}. The leading shell S1 and trailing shell S4 move with ultra-relativistic proper speeds ($u = \Gamma\beta$), $u_4 > u_1 \gg 1$ with $a_u = u_4/u_1 > 1$. The front and back edges of shells (S1, S4) are ejected at times ($t_{ej,f1}$, $t_{ej,b1}$) and ($t_{ej,f4}$, $t_{ej,b4}$), corresponding to the ejection time-scales: $t_{on,i} = t_{ej,bi} - t_{ej,fi}$ for $i = $ (RS, FS). The front edge of shell S4 collides head-on with the back edge of shell S1 at a distance R_o from the central source, and at time t_o where

$$R_o = \frac{\beta_1\beta_4 ct_{off}}{(\beta_4 - \beta_1)} \approx \frac{2\Gamma_1^2 ct_{off}}{1 - a_u^{-2}} , \quad t_o - t_{ej,f4} = \frac{\beta_1 t_{off}}{(\beta_4 - \beta_1)} \approx \frac{R_o}{c} . \quad (1)$$

The collision produces a pair of shocks, where the two shocked parts of shells S1 and S4 are separated by a CD and move with the same proper speed u. The proper speeds of the FS (RS) propagating into shell S1 (S4) satisfy $u_{RS} < u < u_{FS}$. All three proper speeds

remain constant in planer geometry (that we assume here for the dynamics, for simplicity). The shock fronts and CD divide the shells (S1, S4) into four regions (R1, R2, R3, R4). Regions R1/R2 and R4/R3 are the unshocked/shocked parts of shells S1 and S4, respectively. The requirement of equal pressure and velocity across the CD, implies an equal ram pressure across the CD in its rest frame, $u_{21}^2 = f u_{34}^2$ were $u_{ij}^2 = \Gamma_{ij}^2 - 1$, $\Gamma_{21} = \Gamma_2\Gamma_1(1 - \beta_1\beta_2)$ and $\Gamma_{34} = \Gamma_3\Gamma_4(1 - \beta_3\beta_4)$. The shock strength (internal energy per unit rest energy in the shocked region), $\Gamma_{ij} - 1$ where $ij = (21, 34)$, is governed by the proper density contrast, $f = n_4'/n_1'$, which for a constant source power is $\sim a_u^{-2} \ll 1$. This shows that the RS strength ($\Gamma_{34} - 1$) is expected to be larger than the FS strength ($\Gamma_{21} - 1$). The proper velocity of the shocked fluid for an ultra-relativistic flow is $u \approx \Gamma = [(\sqrt{f}a_u^2 + a_u)/(a_u + \sqrt{f})]^{1/2} \Gamma_1$ [see Appendix A (available as online supplementary material)]. The FS reaches the front edge of shell S1 in time t_{FS} while the RS reaches the back edge of shell S4 in time t_{RS}. At the instant ($t_o + t_{FS}$, $t_o + t_{RS}$) the final location of the FS and RS fronts is (R_{FS}, R_{RS}) such that

$$\frac{\Delta R_i}{R_o} = \frac{R_{f,i} - R_o}{R_o} = \frac{\beta_i t_i}{R_o/c} \approx \frac{(1 - a_u^{-2})t_i}{2\Gamma_1^2 t_{off}} \quad \text{for } i = \text{ (RS,FS)} . \quad (2)$$

We account for spherical expansion with a hybrid approach, in which the proper speeds (u, u_{RS}, u_{FS}) remain constant ($\propto R^0$) while the matter density varies as $\rho \propto R^{-2}$. The first assumption allows analytic solutions of the shock crossing times. The second assumption allows us to account for the decrease in density as the shells propagate outward. The shell crossing time-scales are given by (see appendix C of Paper I),

$$t_{RS} = \frac{\beta_4 t_{on4}}{\beta_4 - \beta_{RS}} \approx \frac{2\Gamma^2 t_{on4}}{g_{RS}^2 - \left(\frac{\Gamma}{\Gamma_4}\right)^2} , \quad t_{FS} = \frac{\beta_1 t_{on1}}{\beta_{FS} - \beta_1} \approx \frac{2\Gamma^2 t_{on1}}{\left(\frac{\Gamma}{\Gamma_1}\right)^2 - g_{FS}^2} , \quad (3)$$

where $g_{RS} = \Gamma/\Gamma_{RS} > 1$ and $g_{FS} = \Gamma/\Gamma_{FS} < 1$. For the rest of our analysis, we fix the proper speeds to (u_1, u_4) = (100, 200) corresponding to a proper speed contrast of $a_u = 2$ while our fiducial ratios of the activity and inactivity time-scales are ($t_{on1} : t_{off} : t_{on4}$) = (1 : 1 : 1). Our fiducial case corresponds to the collision of two equal energy shells. We also fix t_{off} which in turn fixes the fiducial collision radius R_o and time t_o. In Section 3, we will explore different combinations of the ratio $t_{on1} : t_{on4}$. We next discuss why even if this ratio is changed arbitrarily, it has a relatively modest effect on the light curves.

For fixed shell proper speeds (u_1, u_4) and a constant source power, the shock front LFs do not change when varying the ejection time-scales, as the proper density contrast f remains unaltered. For an ultra-relativistic flow, the radial width of each shell scales linearly with its ejection duration, $\Delta_i = \beta_i ct_{on,i} \approx ct_{on,i}$, and therefore so does the shock crossing duration t_i. However, a shock cannot always cross the whole shell, for the following reason. The shell crossing time-scales are generally unequal, $t_{RS} \neq t_{FS}$. For example, when $t_{on1} = t_{on4}$ the RS crosses first, $t_{RS} < t_{FS}$. When the RS reaches the back edge of the trailing shell S4, the rear edge of the high-pressure region R3 faces vacuum. This creates a rarefaction (rf) wave that propagates from the vacuum interface into region R3, towards the CD and FS front. If Δ_1 is large enough, the rf wave can catch up with the FS front and stall it, suppressing further internal energy dissipation. Hence, only when $t_{on1}/t_{on4} \approx \Delta_1/\Delta_4$ is sufficiently close to unity can both shocks finish crossing their respective shells. For our setup, this corresponds to the limits $0.42 \leq t_{on1}/t_{on4} \leq 2.68$ (see appendix H of Paper I), beyond which further varying this ratio stops affecting the emission. To respect this limit, for all the illustrations we will restrict the ratio to $0.5 \leq t_{on1}/t_{on4} \leq 2$.

2.2 Synchrotron emission process

As shown in Appendix B (available as online supplementary material), for our moderate fiducial proper speed contrast ($a_u = 2$) the energy dissipation efficiency (defined as the ratio of the internal energy produced to the original total kinetic energy) associated with the RS and the FS is ~ 5 per cent and 3 per cent, respectively. The overall efficiency of ~ 9 per cent is consistent with what has been estimated for plastic collision in internal shock models [Rees & Meszaros 1994; Kobayashi, Piran & Sari 1997; Krimm et al. 2007, see also Appendix B (available as online supplementary material) for a comparison of the hydrodynamic and ballistic approaches]. Moreover, model-independent constraints on the prompt efficiency from combined prompt and afterglow observations give similar estimates (see Beniamini et al. 2015). The observed radiation is from a population of shock-accelerated non-thermal electrons that constitute a fraction ξ_e of all electrons and carries a fraction ϵ_e of the dissipated internal energy density, e'_{int}. A fraction ϵ_B of the dissipated internal energy is carried by the magnetic field, $B'^2/8\pi = \epsilon_B e'_{int}$. Since only a fraction $\epsilon_\gamma = \epsilon_e \epsilon_{rad}$ of the dissipated energy can be radiated, in order to satisfy the observed energetics, it is essential that the radiation be close to the fast-cooling regime ($\epsilon_{rad} \approx 1$). Thus, the RS should be fast cooling or at least not very slow cooling.

To fulfil the energy requirements implied by prompt GRB observations, we assume the fast-cooling regime of optically thin synchrotron emission from non-thermal power-law electrons, with a comoving energy distribution $dn'/d\gamma_e \propto \gamma_e^{-p}$ for $\gamma_m \leq \gamma_e \leq \gamma_M$. The emission is assumed to be isotropic in the comoving frame of the shocked fluid. For simplicity, we assume the microphysical parameters (ϵ_e, ϵ_B, ξ_e, p) to be the same in both shocked regions. As the shock crossing times are similar, the comoving dynamical times are also similar and so is the cooling LF $\gamma_c = 6\pi m_e c/\sigma_T B'^2 t'_{dyn}$, where m_e (m_p) is the electron (proton) mass, c is the speed of light, and σ_T is the Thomson cross-section. The minimum electron LF (for $p > 2$) is given by $\gamma_m = \frac{p-2}{p-1}\frac{m_p}{m_e}\frac{\epsilon_e}{\xi_e}(\Gamma_{ij} - 1) \propto \Gamma_{ij} - 1$, where $ij = (21, 34)$, and is hence higher for the RS compared to the FS. Therefore, we can have $\gamma_m \sim \gamma_c$ in the forward shocked region and $\gamma_m > \gamma_c$ in the reversed shocked region. This gives a natural motivation for choosing a marginally fast cooling ($\gamma_m \sim \gamma_c$) for the forward shocked region R2 and fast cooling ($\gamma_m \gg \gamma_c$) for the reverse shocked region R3. Hereafter, we assume $\epsilon_{rad} = 0.5$ and $\epsilon_{rad} = 1$ for the marginally cooling FS and the fast-cooling RS, respectively. In Section 3, we explore the effects of a fast-cooling FS on the time-integrated spectrum.

2.3 Equal arrival time surfaces

The EATS for each shock front i is defined as the locus of emission points from which photons reach an observer at a given observed time, $T = t - R\cos\theta/c$. For a constant shock front LF Γ_i, the EATS is an ellipsoid with a major to minor axis ratio of Γ_i. The largest radius along the EATS (at $\theta = 0$) is

$$R_{L,i} = \frac{\beta_i c T_{z,i}}{1 - \beta_i} \approx 2c\Gamma_i^2 T_{z,i} \ , \qquad T_{z,i} \equiv \frac{T - T_{ej,i}^{eff}}{1 + z} \ , \qquad (4)$$

[see equation 9 of Appendix F (available as online supplementary material)], where z is the redshift and $T_{ej,i}^{eff}$ is the arrival time of a hypothetical photon emitted at the source at the effective ejection time $t_{ej,i}^{eff}$ of a shell moving at β_i that coincides with the shock at $R \geq R_o$ [see appendices E and F (available as online supplementary material) for details]. The first photons from both shocks reach the observer at T_s, as both are emitted at R_o, t_o, and $\theta = 0$. However, as $\Gamma_{FS} > \Gamma_{RS}$, for our fiducial parameter values the signal from the FS
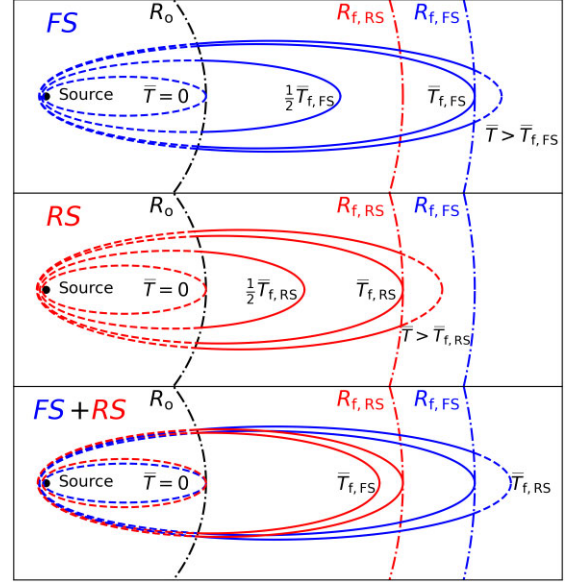

Figure 1. Illustration of the EATS for the time combination $t_{on1} : t_{off} : t_{on4} = (1 : 1 : 1)$. The prescription for construction of EATS is provided in Appendix E (available as online supplementary material). While for the rest of the graphs we use values of $(u_1, u_4) = (100, 200)$, (only) here for illustrating the EATS we use instead $(u_1, u_4) = (3, 6)$ corresponding to $(u_{FS}, u_{RS}) = (4.05, 3.24)$. The EATS major to minor axis ratio is the shock front LF. The black dot corresponds to the compact central source. The observer is located far to the right. The EATS for the FS and RS are shown by blue and red lines, respectively. For a given EATS only the solid portion contributes to the observed emission. Top & middle panels: EATS for the FS & RS, each shown at four instants (see text for explanation). Bottom panel: the combined EATS for both shock fronts (the outer ones belong to the FS while the inner ones belong to RS) at the instants $\overline{T} = (0, \overline{T}_{f,FS}, \overline{T}_{f,RS})$.

fully crossing S1 arrives before that from the RS fully crossing S4, even though $t_{RS} < t_{FS}$.

Fig. 1 shows the EATS due to both shock fronts. We define a normalized time $\overline{T}_i = (T - T_s)/T_{0,i}$, where $T_{0,i} = T_s - T_{ej,i}^{eff}$ such that $\overline{T}_i = 0$ is the time of the first photons from both shocks, emitted at $(R_{L,o}, \theta = 0)$. For display purposes, we use $T_{0,RS}$ as the normalization constant, i.e. use $\overline{T} = \overline{T}_{RS}$; $\overline{T} = \overline{T}_{f,i}$ are the arrival time of photons emitted at $[R_{L,f,i}, \theta = 0$; see Appendix E (available as online supplementary material) for details]. The top and middle panels show the EATS due to both shock fronts at four instants. The times $\overline{T} = (0, 0.5\overline{T}_{f,i}, \overline{T}_{f,i})$ correspond to $R_{L,i} = R_o$, $\frac{1}{2}(R_{f,i} + R_o)$ and $R_{f,i}$. At $\overline{T} > \overline{T}_{f,i}$, we have $R_{L,i} > R_{f,i}$ and the observed flux is dominated by high-latitude emission (HLE; Panaitescu & Kumar 2000), where contributions to the observed flux come from $R_o \leq R \leq R_{f,i}$ corresponding to $\theta_{min} \leq \theta \leq \theta_{max}$ where $\theta_{min} = [2c(T - T_{f,i})/R_{f,i}]^{1/2}$ and $\theta_{max} = [2c(T - T_s)/R_o]^{1/2}$. The bottom panel shows the EATS for both shock fronts at the same three normalized times.

3 RESULTS

The purpose of this present section is to explore the pulse morphology and spectra of GRBs. To calculate the observed flux at a given observed time, we use the formalism of Genet & Granot (2009) and further refine it by distinguishing between the shock front LF, Γ_i, and the shocked matter LF, Γ (common to both the shocked regions), requiring $g_i \neq 1$ (see Section 2.1 for definition). The flux density F_ν received by an on-axis observer from shock i at the normalized time
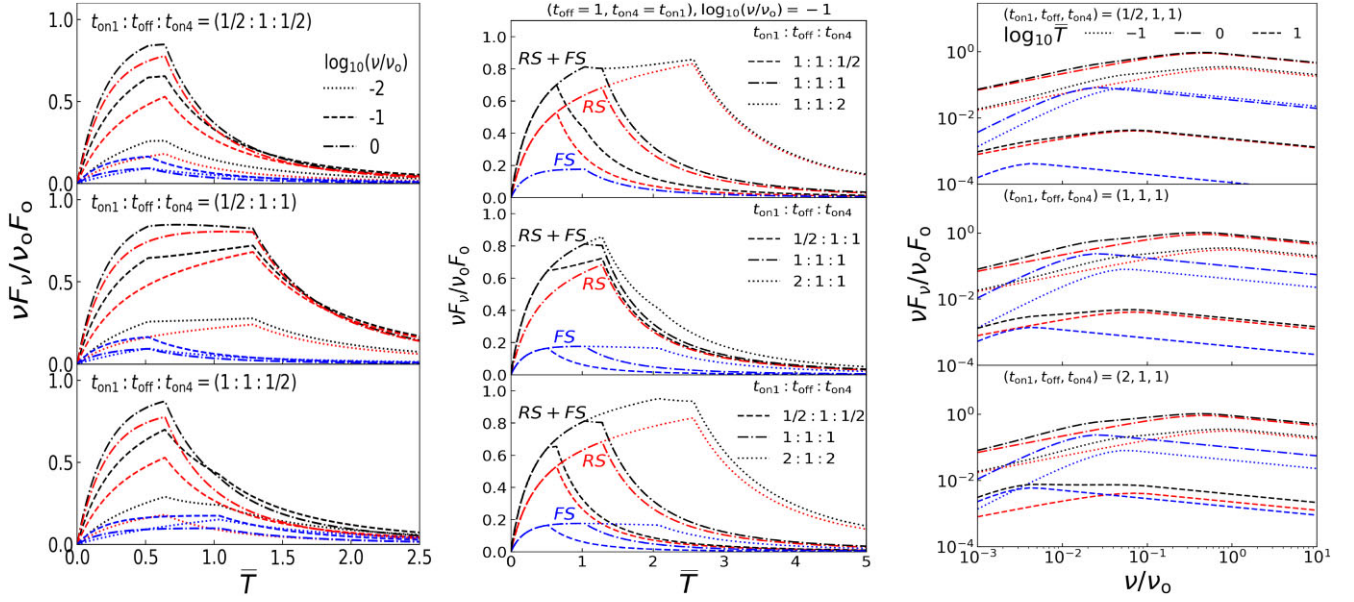
Figure 2. In all panels, red, blue, and black lines correspond to the RS, the FS, and their sum, respectively (see text for details). Left: Light curves at different frequencies. Middle: Light curves at a fixed frequency of $\log_{10}(\nu/\nu_o) = -1$ and varying values of $t_{on1} : t_{off} : t_{on4}$. Right: Time-resolved spectrum at three normalized times. The dotted line, the dot-dashed line, and the dashed line correspond to early, intermediate and late times, respectively (see text for details).
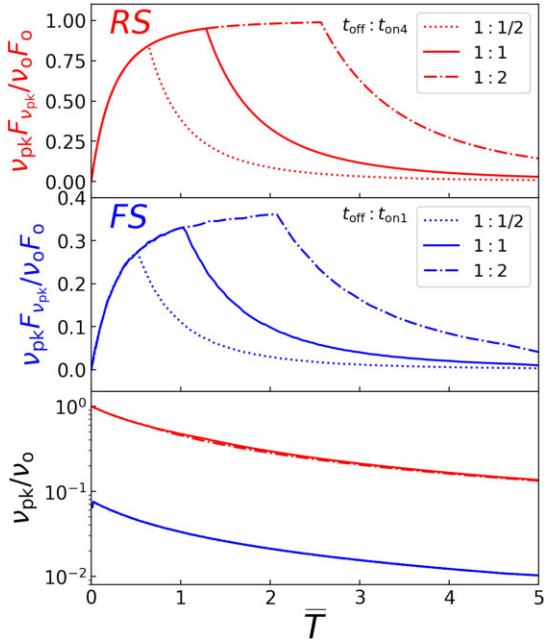

Figure 3. The normalized time evolution of peak luminosity and peak flux. The red and blue lines correspond to the RS and the FS. In the bottom panel the top curves are for RS and the bottom curves are for FS (see text for details).

$\widetilde{T}_i = \overline{T}_i + 1$ is given by

$$\frac{F_\nu}{F_{o,i}}(\widetilde{T}_i) = g_i^2 \widetilde{T}_i \int_{y_{min}}^{y_{max}} dy \, \frac{y^{-1}}{[1 + g_i^2(y^{-1} - 1)]^3} \, S[x] \,, \tag{5}$$

where $y = R/R_{L,i}(\widetilde{T}_i)$ [y_{min}, y_{max} and the full derivation of the expression are described in Appendix F (available as online supplementary material)] where $R_{L,i}$ is the largest radius on the EATS at the normalized time $\widetilde{T}_i = (T - T_{ej,i}^{eff})/T_{0,i}$ [see Appendix E (available as

Table 1. Parameter space (hydrodynamics and synchrotron emission) for both the shocked regions. The proper speeds (u_1, u_4) of shells S1 and S4 are fixed to be 100 and 200, respectively. The indices (b_1, b_2) correspond to the Band function defined in equation (6). The quantity p is the power-law index of the non-thermal electrons and is taken to have the fixed value 2.5. For the FS the quantity ($b_1 = 1/3$, $\epsilon_{rad} = 0.5$) corresponds to the marginally fast-cooling regime of synchrotron emission. For both shocks the combination ($\epsilon_{rad}, b_1, b_2) = (1, -1/2, -p/2)$ corresponds to the very fast-cooling regime of synchrotron emission. The hydrodynamical quantities g_i and shock strength $\Gamma_{ij} - 1$ are defined in Section 2.1.

Shock front	ϵ_{rad}	b_1	b_2	g_i	$\Gamma_{ij} - 1$
FS	0.5 (1)	1/3 (−1/2)	−p/2 = −1.25	0.926	0.027
RS	1.0	−1/2	−p/2 = −1.25	1.155	0.107

online supplementary material)], $F_{o,i} = 2\Gamma(1 + z)L'_{o,i}/4\pi d_L^2$ where d_L is the luminosity distance, z is the redshift, and $L'_{o,i}$ is the peak luminosity in the comoving frame at the collision radii, $x = \nu'/\nu'_p$, where ν' and ν'_p are the comoving frequency and peak frequency respectively, and $S[x]$ is the normalized Band function given by

$$S[x] = e^{1+b_1} \begin{cases} x^{b_1} e^{-(1+b_1)x} & x \leq x_b \\ x^{b_2} x_b^{b_1-b_2} e^{-(b_1-b_2)} & x \geq x_b \end{cases}, \tag{6}$$

where b_1 and b_2 are the asymptotic low and high-frequency spectral slopes, which satisfy $b_1 > -1 > b_2$, and $x_b = (b_1 - b_2)/(1 + b_1) > 1$. Appendix F (available as online supplementary material) gives analytical estimates for the flux from equation (5). For both shocks, the following relationship holds [see Appendices C & D (available in online supplementary material)]

$$\frac{\nu_{o,FS}}{\nu_{o,RS}} \approx \left(\frac{\Gamma_{21}-1}{\Gamma_{34}-1}\right)^2, \quad \frac{F_{o,FS}}{F_{o,RS}} \approx \left(\frac{\epsilon_{rad,FS}}{\epsilon_{rad,RS}}\right) \left(\frac{\Gamma_{34}-1}{\Gamma_{21}-1}\right)^2 \left(\frac{\beta_{21}}{\beta_{34}}\right). \tag{7}$$

The hydrodynamical and emission parameter values for the two shocked regions are given in Table 1. For purposes of display, all the flux, frequency, and observed times are normalized to those of the RS such that $F_o \equiv F_{o,RS}$, $\nu_o \equiv \nu_{o,RS}$, $T_0 \equiv T_{0,RS}$ [see Appendix G

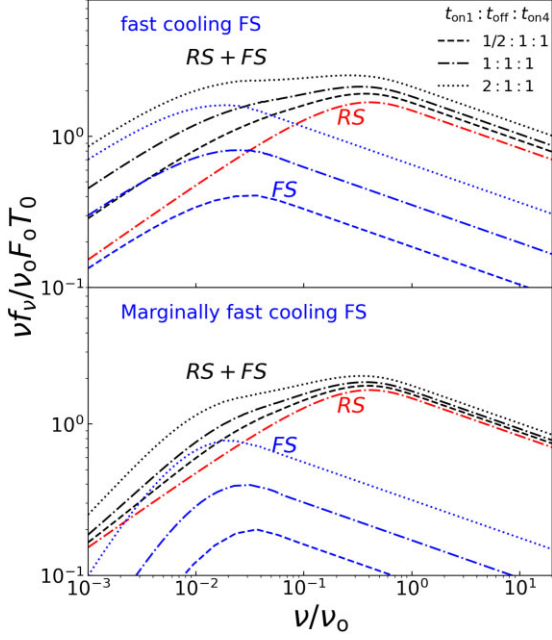**Figure 4.** Time-integrated spectrum for different combinations of $t_{on1} : t_{off}$: t_{on4}. Here $f_\nu = \int dT\, F_\nu(T)$ is the fluence per unit frequency. Top: the spectrum wherein both RS and FS are in the fast-cooling regime. Bottom: the spectrum for a fast-cooling RS and a marginally fast-cooling FS.

(available as online supplementary material)]. For all figures (except Fig. 4), we assume a marginally fast-cooling FS. The RS shock is always in the fast-cooling regime.

The left panels of Fig. 2 show light curves at different frequencies. Each panel displays a fixed time ratio $t_{on1} : t_{off} : t_{on4}$. The pulse from each shock peaks at $\overline{T}_{f,i}$, and the subsequent tail is due to HLE. The total pulse has a particularly complex morphology if $\overline{T}_{f,RS}$ and $\overline{T}_{f,FS}$ are well separated as occurs in middle and bottom panels.

The middle panels of Fig. 2 show the light curves at a fixed frequency. In the top panel, the FS pulse is fixed while the RS pulse is varied by increasing the ejection duration t_{on4} and thus the RS pulse width and peak time. As a result, the total pulse shows a plateau at the limit $t_{on4} \gg t_{off}$. In the middle panel, the RS pulse is fixed and the FS pulse is varied, producing comparatively narrow pulse widths and plateau regions in the observed profile. In the bottom panel, both pulses due to FS and RS are varied and we obtain very large pulse widths and narrow plateaus in the observed profile.

The instantaneous spectrum due to shock front i can be well-modelled by (with an error of less than 1 per cent)

$$(\nu F_\nu)_i = \nu_{pk,i} F_{\nu_{pk},i}\, S\left[\nu/\nu_{pk,i}\right]\,, \tag{8}$$

$$\frac{\nu_{pk,i} F_{\nu_{pk},i}}{\nu_{o,i} F_{o,i}} = \begin{cases} 1 - \widetilde{T}_{eff1,i}^{-3} & \text{for } \widetilde{T}_i \leq \widetilde{T}_{f,i}\,, \\ (1 - \widetilde{T}_{eff1,i}^{-3}|_{\widetilde{T}_{f,i}})\, \widetilde{T}_{eff2,i}^{-3} & \text{for } \widetilde{T}_i \geq \widetilde{T}_{f,i}\,, \end{cases} \tag{9}$$

$$\frac{\nu_{pk,i}}{\nu_{o,i}} = \begin{cases} \widetilde{T}_i^{-1} & \text{for } \widetilde{T}_i \leq \widetilde{T}_{f,i}\,, \\ \widetilde{T}_{f,i}^{-1}\, \widetilde{T}_{eff2,i}^{-1} & \text{for } \widetilde{T}_i \geq \widetilde{T}_{f,i}\,, \end{cases} \tag{10}$$

where the product $\nu_{o,i} F_{o,i}$ is defined in Appendix G (available as online supplementary material) and $S[x]$ is the normalized Band function defined in equation (6) , $\widetilde{T}_{f,i} = R_{f,i}/R_o$, the effective angular time-scales are $\widetilde{T}_{eff1,i} = (1 - g_i^2) + g_i^2 \widetilde{T}_i$ and $\widetilde{T}_{eff2,i} = (1 - g_i^2) + g_i^2 (R_o/R_{f,i})\widetilde{T}_i$ [see Appendix H (available as online supplementary material)] such that $\widetilde{T}_{eff1,i}|_{\widetilde{T}_{f,i}} = (1 - g_i^2) + g_i^2 R_{f,i}/R_o$. In Appendix I (available as online supplementary material), we use our model to

fit $\nu_{pk} F_{\nu_{pk}}$ versus ν_{pk} data for representative GRB samples from Yan et al. (2023). Assuming the peak emission being due to RS we find $\Delta R/R_o$ to be of order unity [see Table I in Appendix I (available as online supplementary material)].

The right panels of Fig. 2 show the peak of the instantaneous spectrum from each shock steadily rises at early times and decays rapidly at later times. At intermediate times the spectra show a double bump structure which becomes more prominent in the integrated spectra. The low frequency bump is due to FS while the high-energy emission is due to RS. While observationally, the low-energy bump is typically interpreted due to be of photospheric origin, our model suggests a weaker FS as a natural alternative candidate (see Section 4).

Fig. 3 shows that the peak flux of the instantaneous $\nu_{pk,i} F_{\nu,pk,i}$ for the shock front i first rises steadily, then reaches a plateau phase and subsequently decays rapidly, while $\nu_{pk,i}$ shows a monotonic hard-to-soft evolution (see Section 4).

Fig. 4 shows the time-integrated spectra which are well-modelled (within an error of less than 4 per cent) as

$$(\nu f_\nu)_i = \nu_{pk,i} f_{\nu_{pk},i}\, S[\nu/\nu_{pk,i}]\,, \tag{11}$$

$$\frac{\nu_{pk,i} f_{\nu_{pk},i}}{\nu_{o,i} F_{o,i} T_{0,i} \overline{T}_{f,i}} = 1.32 - 5.62 \times 10^{-3} \log_{10}\left(\frac{R_{f,i}}{R_o}\right)\,, \tag{12}$$

$$\frac{\nu_{pk,i}}{\nu_{o,i}} = \left[0.805 + 0.706 \left(\frac{R_{f,i}}{R_o}\right)\right]^{-1}\,. \tag{13}$$

The top panel shows the spectra for a fast-cooling FS. In this regime the overall spectrum is consistent with two spectral break fits viz., a high-energy peak and a low energy spectral break. Some studies (e.g. Toffano et al. 2021) indeed favour such doubly broken power-law fits. The bottom panel shows spectra when the FS is marginally fast cooling. The RS is fast cooling in both panels. It can be seen that the low energy bump becomes more prominent if the FS is longer-lived. In this regime, the overall spectra can be well-fit with a Band function for the dominant high-energy peak and a blackbody (BB) like function for the sub-dominant peak. Few studies (e.g. Guiriec et al. 2011, 2013) favour the (Band function + BB) fit. Our model accommodates both kind of fits in a natural way. Both the break in the spectral slope at low energies and a sub-dominant bump are due to a weaker FS in different cooling regimes. The higher energy emission (peak) is dominated by RS.

4 DISCUSSION

We have presented a self-consistent internal shocks model for the prompt GRB emission, accounting for the dynamics and synchrotron radiation of the FS and RS, which naturally explains the variability of the light curves, the temporal behaviour of the instantaneous spectra and the shape of the time-integrated spectrum. These features are obtained from the hydrodynamics alone, since the microphysical parameters (ϵ_e, ϵ_B, ξ_e, p) are taken to be equal in both shocked regions. Any diversity in those parameters will most likely lead to even more diversity in the observed features.

Since an internal collision between two shells generically leads to two shocked regions with distinct physical conditions, our results are distinct from one-zone synchrotron models for GRB internal shocks (Katz 1994; Rees & Meszaros 1994; Daigne & Mochkovitch 1998; Kumar & McMahon 2008; Beniamini & Piran 2013). In the single zone model, there is a conflict. On one hand, the prompt emission energetics require a high-radiative efficiency $\epsilon_{rad} \sim 1$. On the other hand, harder observed spectra, $\alpha \approx -1$ (Kaneko et al. 2006; Nava et al. 2011, 2012; where $\frac{dN}{dE} \propto E^\alpha$), requires

the emission to be in the slow or at most in the marginally fast-cooling regime. These motivated works like (e.g. Daigne, Bosnjak & Dubus 2011; Beniamini, Barniol Duran & Giannios 2018) to consider single zone models involving a marginally fast-cooling regime of synchrotron emission with fine-tuned parameters to achieve the same. In particular, Daigne, Bosnjak & Dubus 2011 show that differential inverse compton (IC) cooling can lead to a low-energy spectral slope that resembles marginally fast cooling. One example of fine tuning is the requirement to have a balance between heating and cooling of electrons which is difficult to maintain continuously and uniformly.

Our model has two emission zones, which are linked by the underlying shock hydrodynamics. In particular, the emission is dominated by the fast-cooling RS while the slope at low energies is determined by the FS. Due to the intrinsic weakness of the FS it may naturally be in the slow/marginally fast-cooling regime. As it is sub-dominant this does not affect the overall efficiency, which is dominated by the RS. The overall spectrum is the sum of the emission from the two shocks, and can therefore exhibit a doubly broken power law. The lowest energy power-law index can be $\alpha \approx -2/3$ from a slow-cooling FS. The intermediate segment can be $-2 \lesssim \alpha \leq -3/2$ (between the peaks of the emission from the two shocks). The highest energy segment is $\alpha = -(p + 2)/2$ dominated by the RS. Indeed such spectral models have been successfully fit to prompt GRB data (e.g. Burgess et al. 2014; Oganesyan et al. 2017; Ravasio et al. 2019).

Moreover, for the low-energy bump in the time-integrated spectrum, which is usually interpreted as a quasi-thermal optically thick 'photospheric' component (see Guiriec et al. 2017 and the references therein), we find an alternative explanation as an optically thin 'non-thermal' emission from the relatively weaker FS. The observed spectrum both at the low- and high-energy ends is dominated by the more powerful RS. It is possible that at least in some cases the low-energy bump has contribution from a photospheric component as well. However, if the contribution from the FS dominates, it implies a sub-dominant photospheric contribution. Observational fits to the time-resolved and time-integrated spectra using equations (8)–(10) and (11)–(13), respectively, will provide more robust constraints on the ratio of the shock strengths.

In our model, there is a monotonic hard to soft evolution of the peak photon energy. In Appendix I (available as online supplementary material), we show how the $\nu_{pk} F_{\nu_{pk}}$ versus ν_{pk} data can be exploited to infer $\Delta R/R_0$ in our model. However, in some GRBs ν_{pk} follows $\nu_{pk} F_{\nu_{pk}}$, referred to as intensity tracking (Golenetskii et al. 1983; Liang & Kargatis 1996; Lu et al. 2012). Beniamini & Granot (2016) show that intensity tracking can be reproduced when the GRB energy dissipation is driven by magnetic reconnection. Thus, intensity tracking may point to a different underlying physics.

One may potentially distinguish between a true photospheric emission and a non-thermal photospheric-like emission from the FS. The true photospheric emission arises much closer to the source, leading to an earlier onset time – a precursor emission to each pulse, which may be detectable in particularly bright pulses. It will also have a sharper spectral peak and a harder low-energy photon index.

Finally, we point out a few limitations of our current study. We have assumed a moderate proper speed contrast ($a_u = 2$), which roughly reproduces the observed ratio of the peak photon energies, $E_{pk,RS}/E_{pk,FS} \sim 10$–$10^{1.5}$. However, this ratio scales as the square of the shock strengths, $E_{pk,RS}/E_{pk,FS} \propto (\Gamma_{34} - 1)^2/(\Gamma_{21} - 1)^2$, and can become very large for $a_u \gg 1$, which is not observed. However, this may be mitigated by accounting for the effects of the spherical geometry on the shock dynamics, which are expected to reduce the ratio of shock strengths and thereby also $E_{pk,RS}/E_{pk,FS}$ with R/R_o and

time. The thin shell instantaneous emission region approximation may also break for a marginally fast-cooling FS. Shock propagation in a spherical geometry, larger proper speed contrasts, and a finite instantaneous emission region will be pursued in a future study.

DATA AVAILABILITY

No new data were generated during the analysis of this project.

REFERENCES

Beniamini P., Granot J., 2016, MNRAS, 459, 3635
Beniamini P., Piran T., 2013, ApJ, 769, 69
Beniamini P., Nava L., Duran R. B., Piran T., 2015, MNRAS, 454, 1073
Beniamini P., Barniol Duran R., Giannios D., 2018, MNRAS, 476, 1785
Bosnjak Z, Daigne F., Dubus G., 2009, A&A, 498, 677
Burgess J. M. et al., 2014, ApJ, 784, 17
Bustamante M., Heinze J., Murase K., Winter W., 2017, ApJ, 837, 33
Daigne F., Mochkovitch R., 1998, MNRAS, 296, 275
Daigne F., Bosnjak Z, Dubus G., 2011, A&A, 526, A110
Genet F., Granot J., 2009, MNRAS, 399, 1328
Golenetskii S. V., Mazets E. P., Aptekar R. L., Ilinskii V. N., 1983, Nature, 306, 451
Granot J., 2005, ApJ, 631, 1022
Granot J., Cohen-Tanugi J., Silva E. d. C. e., 2008, ApJ, 677, 92
Guetta D., Spada M., Waxman E., 2001, ApJ, 557, 399
Guiriec S. et al., 2011, ApJ, 727, L33
Guiriec S. et al., 2013, ApJ, 770, 32
Guiriec S., Gehrels N., McEnery J., Kouveliotou C., Hartmann D. H., 2017, ApJ, 846, 138
Kaneko Y., Preece R. D., Briggs M. S., Paciesas W. S., Meegan C. A., Band D. L., 2006, ApJS, 166, 298
Katz J. I., 1994, ApJ, 432, L107
Kobayashi S., Piran T., Sari R., 1997, ApJ, 490, 92
Krimm H. A. et al., 2007, ApJ, 665, 554
Kumar P., McMahon E., 2008, MNRAS, 384, 33
Liang E., Kargatis V., 1996, Nature, 381, 49
Lu R.-J., Wei J.-J., Liang E.-W., Zhang B.-B., Lü H.-J., Lü L.-Z., Lei W.-H., Zhang B., 2012, ApJ, 756, 112
Nakar E., Piran T., 2002, MNRAS, 331, 40
Nava L., Ghirlanda G., Ghisellini G., Celotti A., 2011, A&A, 530, A21
Nava L. et al., 2012, MNRAS, 421, 1256
Oganesyan G., Nava L., Ghirlanda G., Celotti A., 2017, ApJ, 846, 137
Panaitescu A., Kumar P., 2000, ApJ, 543, 66
Rahaman S. M., Granot J., Beniamini P., 2023, Internal Shocks Hydrodynamics: the Collision of Two Cold Shells in Detail, preprint (arXiv:2309.16327) (Paper I)
Ravasio M. E., Ghirlanda G., Nava L., Ghisellini G., 2019, A&A, 625, A60
Rees M. J., Meszaros P., 1994, ApJ, 430, L93
Rudolph A., Bosnjak Z, Palladino A., Sadeh I., Winter W., 2022, MNRAS, 511, 5823
Rudolph A., Petropoulou M., Bosnjak Z, Winter W., 2023, ApJ, 950, 28
Sari R., Piran T., 1997, MNRAS, 287, 110
Spada M., Panaitescu A., Mészáros P., 2000, ApJ, 537, 824
Toffano M., Ghirlanda G., Nava L., Ghisellini G., Ravasio M. E., Oganesyan G., 2021, A&A, 652, A123

Yan Z.-Y., Yang J., Zhao X.-H., Meng Y.-Z., Zhang B.-B., 2023, preprint (arXiv:2308.00772)

SUPPORTING INFORMATION

Supplementary data are available at *MNRASL* online.

suppl_data

Please note: Oxford University Press is not responsible for the content or functionality of any supporting materials supplied by the authors.

Any queries (other than missing material) should be directed to the corresponding author for the article.

This paper has been typeset from a TEX/LATEX file prepared by the author.